

Research Article

Geomagnetic Energy Approach to Space Debris Deorbiting in a Low Earth Orbit

Guanhua Feng,^{1,2} Wenhao Li^{1,2} ,^{1,2} and Heng Zhang^{1,2}

¹*Institute of Mechanics, Chinese Academy of Sciences, Beijing 100190, China*

²*School of Engineering Sciences, University of Chinese Academy of Sciences, Beijing 100049, China*

Correspondence should be addressed to Wenhao Li; liwenhao@imech.ac.cn

Received 13 April 2018; Revised 7 August 2018; Accepted 29 August 2018; Published 7 February 2019

Academic Editor: Paolo Tortora

Copyright © 2019 Guanhua Feng et al. This is an open access article distributed under the Creative Commons Attribution License, which permits unrestricted use, distribution, and reproduction in any medium, provided the original work is properly cited.

The space debris removal problem needs to be solved urgently. Over 70% of debris is distributed between the 500 km and 1000 km low Earth orbits (LEO), and existing methods may be theoretically feasible but are not the high-efficiency and low-consumption methods for LEO debris removal. Based on the torque effect of a static magnet interacting with the geomagnetic field, a new spin angular momentum exchange (SAME) method by geomagnetic excitation (without working medium consumption) for LEO active debris deorbiting is proposed. The LEO delivery capability of this method is researched. Two kinds of spin angular momentum accumulation (SAMA) strategies are proposed. Then through numerical simulation under the dipole model and International Geomagnetic Reference Field (IGRF11) model, the results confirm the physical feasibility and basic performance of the proposed method. The method can be applied to the regions of the LEO below 1000 km with different altitudes/inclinations and eccentricities, and with existent magnetorquer technology, only several days of preparation is required for about 10^4 m·kg mechanism-scale-debris-mass deorbiting, which can be used for deorbiting missions in debris-intensive areas (altitude ≤ 1000 km); without consideration of external effects on the geomagnetic field distribution, it has the same deorbiting capability with that of the LEO below 1000 km when the altitude is over 1000 km. Besides, the method is characterized by explicit mechanism, flexible control strategy and application, and low dependence on the scale. Finally, the key technology requirements and future application of LEO active debris removal and on-orbit delivery by using SAME are prospected.

1. Introduction

Since the Soviet Union launched the first satellite in 1950s, space debris increases rapidly in the low Earth orbit (LEO) with the increasing frequent space activities of human beings [1, 2]. The scenario of the high density of debris is such that collisions between debris increase not only the debris population but also the probability of further collisions, known as Kessler syndrome, creating a debris belt around the Earth [3]. The data of orbital population till July 26, 2018, from SATCAT Boxscore [4] is listed in Table 1, and the total has reached 43578. Studies by Liou in Ref. [5] show that mass distribution in the LEO concentrates in three regions, namely, the altitude of around 600 km, 800 km, and 1000 km, and that 99% of the total mass in the orbit is 10 cm and larger debris; besides, studies at ESA (European Space Agency) also indicate that the most densely populated region in the LEO is

at the altitude of about 800–1000 km with high inclinations, i.e., 800 km and 98° inclination, 850 km and 71° inclination, and 1000 km and 82° inclination [6]. Natural decay approaches, such as “the 25-year rule” [7] and raising debris to a graveyard orbit [8] or limiting the launch rate, are neither feasible nor helpful for retrieval/removal of debris [6]. Therefore, techniques of active debris removal (ADR) and capturing in the LEO were proposed and studied over the past two decades [9, 10] and we will discuss as follows.

The most promising ADR or capturing approaches that we introduce here are tethered space systems (TSS), propulsion systems, robotic arm, drag augmentation systems, and other contactless removal approaches [2, 9, 10]. The TSS generally include a tethered space net (TSN), a tethered space gripper (TSG), a tethered space harpoon (TSH) [11], electrodynamic tethers (EDT) [12], and a momentum exchange tether (MET), where TSN, TSG, and TSH, which are named

TABLE 1: Orbital population till July 26, 2018.

Source	Payloads				Debris			All		
	OD	D	T	A	OD	D	T	OD	T	
All	4824	3310	8134	2019	14362	21082	35444	19186	24392	43578

OD: on orbit; D: decayed; T: total; A: active.

as a tethered space robot (TSR) [12] and belong to debris capturing approaches [9], consist of three main parts [11]: base satellite, tether, and subsatellite; the subsatellite released using a spring ejection device is part of the base satellite until deployment, and the base satellite and subsatellite are connected by a tether [13]. The best known ADR mission called e.Deorbit of ESA's Clean Space initiative [10] will launch a derelict satellite in the LEO in 2023 and use the concept of TSN [14]. For the preparation work of e.Deorbit, Gołębowski et al. in Ref. [15] developed a simulator to aid net design and scenario evaluation for debris deorbiting and corresponding verification experiments in microgravity conditions were carried out on board of a Falcon-20 aircraft. For the dynamics and control of the TSS, there are two key problems needed to be solved, i.e., the suppression of spinning debris and the vibration of the tether [16]. Zhang et al. in Ref. [16] firstly gave the precise 3D mathematical model and relative motion equation of the TSS and then designed an offset control law to suppress the spin of debris. In recent years, Huang and his team have built the dynamics model and achieved a series of control strategies to suppress the vibration of the tether for the TSN and TSG. Considering the external disturbances, they completed the derivation of the dynamics model of TSG in Ref. [11], and an improved control algorithm of super-twisting sliding mode control (STSMC) was proposed to eliminate the vibration of the tether in the station-keeping phase. In Ref. [17], the dynamics equations of TSN's flexibility and elasticity are derived and a modified adaptive STSMC was proposed for TSN stability control, which can effectively suppress oscillations. To address the problem of net shape maintenance during deployment, they proposed a distributed coordination control scheme for TSN in Ref. [12]; also, a monocular visual serving control method is proposed in Ref. [1] for the altitude control of TSG in the ultraclose approaching phase. The work by Reed and Barraclough [18] demonstrated the viability of the concept of TSH, and Dudziak et al. in Ref. [19] confirmed the effectiveness of the application of TSH by empirical testing and numerical modeling. EDT is classed as an ADR approach [10] and is part of the tether propulsion systems with low cost [20]. Based on the interaction effect with the geomagnetic field, electrodynamic thrust/drag is generated for changing the altitude of debris to achieve the orbit transfer or orbital debris removal [20]. The greatest merit of EDT is that the tether can generate electrodynamic force for a very long duration without or with little mass consumption [21] but a tether with long kilometer-level length dramatically increases the probability of quadratic collision [22]. The feasibility and implementability of EDT have been invalidated by a large number of well-known space missions, including TSS-1 [23] proposed by NASA

in 1992, Plasma Motor Generator (PMG) [24] experiment of NASA in 1993, TSS-1R [25] (a follow-up mission to TSS-1) in 1996, and EDT of Japan Aerospace Exploration Agency (JAXA). Substantial works have been done on the dynamics and control of EDT. Yu et al. in Ref. [26] built three typical deployment dynamics models of EDT, including the continuous model, discrete model, and rod model; also, control methods and the corresponding control laws of the tether deployment were discussed in detail, such as length control, length rate control, tension control, and thruster control. Under the dumbbell assumption, the attitude dynamics of the EDT system was modeled by a nonsingular formulation in Ref. [27] and a feedback control law of the electric current is designed to stabilize the attitude motions. However, the coupling effect of the tether deflection and electrodynamic force [28] is inevitable in the EDT system. To solve the tether dynamics and orbital motional limited (OML) theory simultaneously, Li and Zhu in Ref. [29] developed a multiphysics finite element method for the dynamic analysis of debris deorbiting by a flexible EDT and discussed the influence of the environment and tether parameters on the electron collection efficiency in Ref. [28]. Besides EDT, MET is also an important ADR method without working medium consumption [30]. Due to altitude difference, there is a relative velocity between the spacecraft in the system to tension the tether. As the tether is separated, the altitude of the spacecraft in the lower orbit drops, while the altitude of the spacecraft in the higher orbit rises, so that the spacecraft will complete momentum exchange. Space experiments on MET systems have been carried out [31], such as the Russian Tether-1, Tether-1A. Due to the same scale features of MET and EDT, Momentum-Exchange/Electrodynamic Reboost (MXER) tether project [32, 33] proposed by American Sorensen, and satellite capture, repair, and removal systems for noncooperative satellites proposed by Japanese Ishige, all have the characteristics of the combination of EDT and MET. Whether it is the EDT or MET systems, its performance depends on the tether scale. And with the vast scale from thousands of meters to tens of kilometers, the stable operation reliability problem of the tether system becomes very prominent [31].

Propulsion systems are also important approaches to ADR and usually consist of chemical propulsion, hybrid propulsion, electrical propulsion, laser propulsion, and others [2, 34]. A propulsion system generally consists of a power source and a propulsor to generate propulsive force for ΔV requirements of orbit transfer or debris deorbiting, and its performance is strongly affected by system volume, system mass, and cost of the propulsion unit [35]. Tadini et al. in Ref. [35] presented in detail the preliminary design and mass budget of chemical propulsion and hybrid propulsion modules and

concluded that under the identical removal requirements, the solid propulsion motor can lead to a very compact system with a lower wet mass than that of a liquid/hybrid propulsion motor [22, 35]. An electrical propulsion system uses electrical energy usually generated by solar panels (i.e., solar electrical propulsion (SEP) [36]) or electrically expelling propellant (i.e., working mass) to meet deorbiting velocity requirements, and its principle is different with those of EDT systems by the interaction with the geomagnetic field [22]. The propellant mass consumption of the electrical propulsion is much less than that of the chemical propulsion because of its higher exhaust speed [37], and space systems with electrical propulsion can run steadily in a long period. But thrust force generated by the electrical propulsion is much weaker than that of the chemical propulsion [38]. The ESA's SMART-1 Project in 2004 completed a one-year mission extension and demonstrated the key techniques and capability of the spacecraft with the electrical propulsion [39]. Ruggiero et al. in Ref. [37] completed the preliminary ADR mission analysis and designed the spacecraft of a small electrical propulsion platform for a deorbiting mission. Also, they validated that by using the high-specific-impulse electrical propulsion system, they can save a great deal of propellant mass. Laser propulsion is a contactless removal approach [10] and can be segmented into two kinds of common approaches, i.e., pulse laser propulsion (PLP) and continuous wave propulsion (CWP) [34]. Based on the ground- or space-based energy source, counterforce is exerted on the material surface of the target object for momentum transition; PLP therefore has a very outstanding merit compared to all other propulsion approaches, which can increase the payloads and decrease the launch costs of space missions [34].

Robotic arm technique has been developed rapidly and was initially used for on-orbit servicing missions [10]. The DLR's DEOS (Deutsche Orbitale Servicing Mission) [40] is a project of robotic arm technique for the end-of-life spacecraft disposal, and Ref. [40] discussed its mission objective, task, and space segment and demonstrated the entire process from rendezvous to deorbiting. When capturing a noncooperative target, the robotic arm must take a few problems into major consideration, including impact influence minimization, detumbling, and altitude synchronization [9, 10]. Liu et al. established the kinematics and dynamics models of the multiarm chaser, floating target, and chaser target in Ref. [41] and proposed a whole-body compliant control strategy based on the Cartesian space impedance behavior and a multiarm force distribution approach to enhance the chaser-target system performance and stability. In Ref. [42], an autonomous trajectory planner based on the teleprogramming framework is developed by Zhang and Liu for debris capturing by a space manipulator; also, Mu et al. in Ref. [43] built a unified modeling framework for multiple moving space targets and proposed a collision-free trajectory planning approach based on the pseudodistance for a redundant manipulator. Considering the system uncertainties, Shi et al. in Ref. [44] studied the coordinated control of the base attitude and arm motion for a dual-arm space robot system, and by simulation examples, they discussed the characteristics of three controllers in respect to control accuracy and

system robustness, such as the computed torque controller (CTC), sliding mode controller (SMC), and nonlinear model predictive controller (MPC).

Drag augmentation systems are passive deorbiting approaches by manually increasing the area-mass ratio of space debris [10], such as expanding foam approach [45], inflated method [7], and solar radiation augmentation sail [46]. The technique eliminates working mass consumption for deorbiting propulsion, but it consumes installation materials, and the required deorbiting time takes several months, greatly increasing the quadratic collision probability [9]. In addition to the abovementioned laser propulsion approach, ion-beam shepherd (IBS) is another important contactless approach and the hovering satellite (i.e., shepherd) generates thrust force on the space debris by the ion beam at high speed [21]. Cichocki et al. studied the satellite-plasma-debris interaction of the ADR mission based on the IBS concept in Ref. [47] and proposed an optimization design point for the subsystem of the IBS systems in Ref. [48].

In summary, LEO space debris removal is a prominent problem pressed for solution. And it is hard to find a good solution to meet all requirements simultaneously, including economy (low consumption), safety (rapid deorbiting and small scale), and maneuverability. In this paper, we first propose a new momentum exchange (we call it the spin angular momentum exchange (SAME)) method by geomagnetic excitation for LEO space debris deorbiting in Section 2. Section 3 treats its capability estimation, and Section 4 presents two strategies for spin angular momentum accumulation (SAMA) of the spacecraft debris system and analyzes the corresponding deorbiting capability. Then by simulation examples in Section 5, the feasibility, performance, and application scope of the proposed method are discussed. In Section 6, the required key technology of the proposed method is analyzed. The conclusion and prospect are discussed in Section 7.

2. SAME Method by Geomagnetic Excitation

The conversion of the spin angular momentum to linear momentum is also one of the means of space momentum exchange, and this momentum exchange thought was reflected in the Soviet Union Tsiolkovski's book in 1895 and spin tether space station design project proposed by Kondratyuk in the 1930s. The momentum exchange using altitude difference takes advantage of the potential energy of the Earth's gravitational field; so, as long as the altitude difference is large enough (i.e., the tether is long enough), enough momentum can be exchanged, while the SAME amount depends on the magnitude of the angular momentum injected into the system. The flywheel or control moment gyros (CMG) are limited by their own inertia and angular velocity upper limit and cannot be injected with a large angular momentum. And the jet-propelled angular momentum injection method is costly, and the detumbling problem is very serious [49]. The above constraints may be the important reason to limit the further research and development of space SAME in recent years.

On the basis of the effect that the magnet in the geomagnetic field is affected by magnetic force and magnetic torque, magnetorquer has been well developed and applied in the

navigation and altitude adjustment/stabilization of the LEO spacecraft and unloading of the torque control mechanisms (such as flywheel). Accordingly, when magnetic intensity (magnitude and direction) is controlled actively, it can become the angular momentum injection resource of the SAME system. The magnetic torque of the magnet in the geomagnetic field is as follows:

$$\mathbf{L} = \mathbf{m} \times \mathbf{B}, \quad (1)$$

where \mathbf{L} denotes the magnetic torque vector, \mathbf{m} denotes the magnetic moment vector carried by the delivery spacecraft, and \mathbf{B} denotes the geomagnetic field intensity vector. From equation (1), the magnet can obtain the required torque only after charging and adjusting its magnetic moment vector (direction or magnitude), unlike the flywheel whose system angular momentum injection relies on the spin angular velocity increment. So, there is no upper limit in theory for the injection amount of system angular momentum. Given enough time and with gradual accumulation, the amount of the injectable angular momentum is considerable.

So, the method that we propose for LEO space debris deorbiting is that based on the torque effect of the electromagnet carried by the delivery spacecraft in the geomagnetic field, and by active SAMA strategy, the angular momentum can be injected into the spin spacecraft debris system powered by solar energy. When the angular velocity reaches the deorbiting requirement, space debris on-orbit delivery can be completed by the reasonable choice of deorbiting time and orientation angle, as shown in Figure 1.

3. Deorbiting Capability Estimation

3.1. Definitions of Coordinates. Figure 2 shows the geomagnetic distribution coordinates $OX_m Y_m Z_m$. And its origin O is located in the mass center of the spacecraft, the X_m -axis points to the north, the Y_m -axis points to the east, and the Z_m -axis points to the Earth's center.

In Figure 2, where $OX_i Y_i Z_i$ denotes the geocentric-equatorial inertial coordinates, $OX_o Y_o Z_o$ denotes the orbital coordinates, i denotes the inclination, α denotes the right ascension, Ω denotes the right ascension of the ascending node, N denotes the ascending node, and u denotes the argument of the ascending node (i.e., the sum of the argument of perigee ω and true anomaly f). When the inclination is i , the conversion matrix of geomagnetic coordinates to orbital coordinates is shown as follows:

$$\mathbf{R}_{om} = \begin{bmatrix} \sin i \cdot \cos \kappa & \sqrt{1 - \sin^2 i \cdot \cos^2 \kappa} & 0 \\ -\sqrt{1 - \sin^2 i \cdot \cos^2 \kappa} & \sin i \cdot \cos \kappa & 0 \\ 0 & 0 & 1 \end{bmatrix}, \quad (2)$$

where κ is the projection angle of the argument of the ascending node u on the equatorial plane.

3.2. LEO Space Magnetic Field Distribution and Deorbiting Mechanism. In the LEO (orbital altitude ≤ 1000 km) space,

the steady-state exterior geomagnetic field intensity is less than one-thousandth of the intensity of the interior geomagnetic field, while under strong disturbance, the exterior geomagnetic field intensity is usually less than one percent of the interior geomagnetic field intensity. So, only the Earth's interior geomagnetic field is taken as the magnetic field model. In Ref. [50], the distribution characteristics of the Earth's magnetic field intensity and the magnetic field intensity gradient environment are deduced in detail and the distribution difference between the dipole model and IGRF model is discussed. For the convenience in analysis, the magnetic dipole whose magnetic north points to the geographic South Pole, in this paper, is used as the simplified geomagnetic field model (i.e., dipole model). In simulation examples below, the IGRF11 model is added for verification.

Based on the dipole model, the components of magnetic intensity in the geomagnetic distribution coordinates are shown as follows:

$$\begin{cases} B_x = \frac{\mu_0 m_e \cos \varphi}{4\pi r^3}, \\ B_y = 0, \\ B_z = \frac{\mu_0 m_e \sin \varphi}{2\pi r^3}, \end{cases} \quad (3)$$

where $m_e (= 8.0 \times 10^{22} \text{ Am}^2)$ is the Earth's magnetic moment, φ is the geographic latitude, r is the geocentric distance, and $\mu_0 (= 4\pi \times 10^{-7} \text{ N} \cdot \text{A}^{-2})$ is the permeability of vacuum. And the magnetic intensity gradient tensor matrix is as follows:

$$\begin{bmatrix} \frac{\partial B_x}{r \partial \varphi} & \frac{\partial B_y}{r \partial \varphi} & \frac{\partial B_z}{r \partial \varphi} \\ \frac{\partial B_x}{r \partial \lambda} & \frac{\partial B_y}{r \partial \lambda} & \frac{\partial B_z}{r \partial \lambda} \\ \frac{\partial B_x}{\partial r} & \frac{\partial B_y}{\partial r} & \frac{\partial B_z}{\partial r} \end{bmatrix} = \begin{bmatrix} -\frac{\mu_0 m_e \sin \varphi}{4\pi r^4} & 0 & \frac{\mu_0 m_e \cos \varphi}{2\pi r^4} \\ 0 & 0 & 0 \\ \frac{3\mu_0 m_e \cos \varphi}{4\pi r^4} & 0 & \frac{3\mu_0 m_e \sin \varphi}{2\pi r^4} \end{bmatrix}. \quad (4)$$

Equations (5) and (6) are the force and torque, respectively, of the magnet with a magnetic moment of m in the Earth's magnetic field. Based on the simplified geomagnetic field model (i.e., dipole model), equations (5) and (6) can be simplified into equations (7) and (8), respectively [50].

$$\begin{aligned} \mathbf{F}^m &= (\mathbf{m} \cdot \nabla) \mathbf{B} = \frac{1}{r} \left(m_x \frac{\partial B_x}{\partial \varphi} + m_y \frac{\partial B_y}{\partial \varphi} + m_z \frac{\partial B_z}{\partial \varphi} \right) \mathbf{i} \\ &+ \frac{1}{r \cos \varphi} \left(m_x \frac{\partial B_x}{\partial \lambda} + m_y \frac{\partial B_y}{\partial \lambda} + m_z \frac{\partial B_z}{\partial \lambda} \right) \mathbf{j} \\ &- \left(m_x \frac{\partial B_x}{\partial r} + m_y \frac{\partial B_y}{\partial r} + m_z \frac{\partial B_z}{\partial r} \right) \mathbf{k}, \end{aligned} \quad (5)$$

$$\begin{aligned} \mathbf{L}^m &= \mathbf{m} \times \mathbf{B} = (m_y B_z - m_z B_y) \mathbf{i} + (m_z B_x - m_x B_z) \mathbf{j} \\ &+ (m_x B_y - m_y B_x) \mathbf{k}, \end{aligned} \quad (6)$$

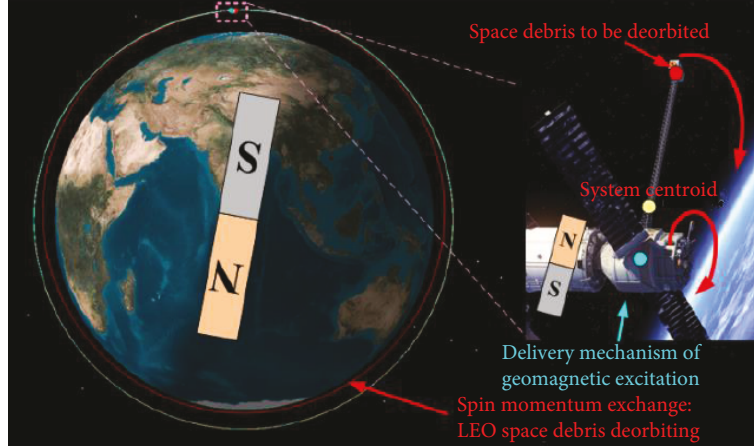


FIGURE 1: Diagram of LEO space debris deorbiting by geomagnetic excitation.

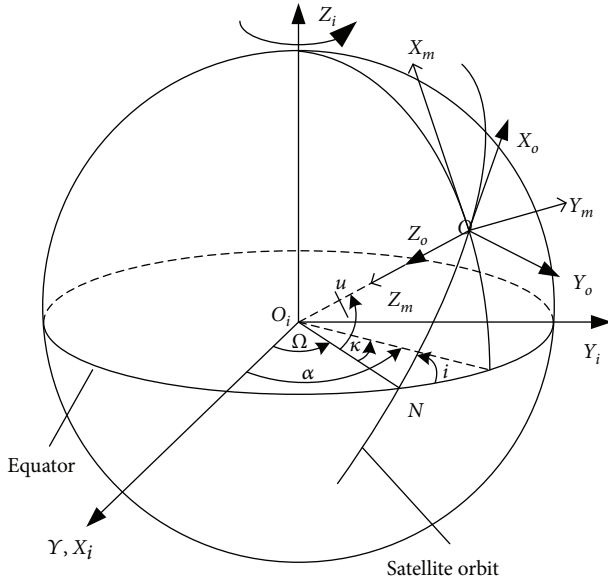


FIGURE 2: Definitions of coordinate systems.

where $m = [m_x, m_y, m_z]$, m_x , m_y , and m_z are the components of the magnetic moment in the geomagnetic distribution coordinates and the superscript m of the force \mathbf{F}^m and torque \mathbf{L}^m denotes that they are described in the geomagnetic distribution coordinates.

$$\mathbf{F}^m = \frac{1}{r} \left(m_x \frac{\partial B_x}{\partial \varphi} + m_z \frac{\partial B_z}{\partial \varphi} \right) \mathbf{i} - \left(m_x \frac{\partial B_x}{\partial r} + m_z \frac{\partial B_z}{\partial r} \right) \mathbf{k}, \quad (7)$$

$$\mathbf{L}^m = m_y B_z \mathbf{i} + (m_z B_x - m_x B_z) \mathbf{j} - m_y B_x \mathbf{k}. \quad (8)$$

3.3. Deorbiting Capability Estimation. For convenience, the delivery spacecraft and the space debris to be delivered are regarded as particle. Assume that the mass of the delivery spacecraft is M_1 , the mass of the space debris to be deorbited is M_2 , and the two are connected by a rigid rod; the length of the rigid rod is R and its mass is negligible. As shown in Figure 3, the delivery spacecraft and the debris rotate around the system mass center under the magnetic torque \mathbf{L} and the

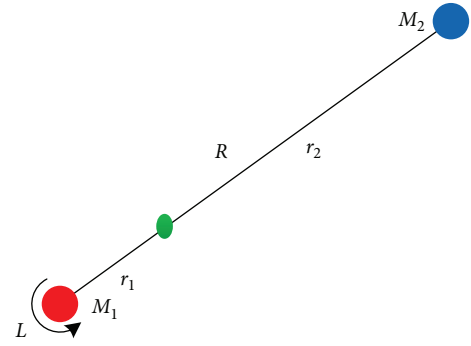


FIGURE 3: Diagram of the deorbiting system model.

distance r_1 from the spacecraft to the system centroid and the distance r_2 from the space debris to the system centroid satisfy the equation $M_1 \cdot r_1 = M_2 \cdot r_2$. Assume that the required velocity change of the debris to be deorbited is ΔV . Under the condition of zero initial spin angular momentum of the system, according to the moment of momentum theorem, the deorbiting condition that the space debris can meet must satisfy the following:

$$\Delta V = \int_0^T \dot{\omega} dx \cdot r_2 = \frac{\int_0^T L(t) dt}{M_1 r_1^2 + M_2 r_2^2} = \frac{\int_0^T L(t) dt}{M_2 R}, \quad (9)$$

where T and $L(t)$ are the required time and angular momentum accumulation, respectively, meeting the deorbiting condition.

Assuming that the deorbiting aim is to reduce the perigee altitude to 150 km, Table 2 is the required deorbiting velocity changes in different circular orbit altitudes and the results is from the orbit simulation software.

From the analysis of the LEO space magnetic field that we know [51], the magnetic intensity in the entire regions of LEO space is greater than 10^{-5} T. With the existing technology, we can generate the 10^5 Am² level stable, controllable, light-weight, and low-power magnetorquer (in 2005, the electromagnetic formation flight (EMFF) technique of the Massachusetts Institute of Technology (MIT) was achieved

TABLE 2: The required velocity changes in different altitudes.

Altitude (km)	Deorbiting velocity changes (m/s)
900	204 (from 7400.5 to 7196.8)
800	178 (from 7451.5 to 7273.0)
700	153 (from 7504.3 to 7351.2)
600	127 (from 7557.9 to 7430.9)
500	101 (from 7612.6 to 7512.7)

by driving current through three orthogonal electromagnetic coils powered by solar energy to create a 3D steerable magnetic dipole; the coil radius is 1 m, and the total mass is 10 kg, which generates a magnetic moment of 0.622×10^5 A m² [52, 53]), which can create a 1 Nm–10 Nm level injectable magnetic torque. We also assume that the mass M_2 is 10 kg, and the distance R between the spacecraft and the debris is 10 m. From equation (9), when the average $L(t)$ reaches 1 Nm, taking the deorbiting in the 900 km circular orbit as an example, we can obtain the estimation results that the required angular momentum accumulation reaching to the deorbiting velocity of the target is 2.04×10^4 Nms and the corresponding accumulated time is 2.04×10^4 s, less than the 2.5 orbital period.

4. Spin Angular Momentum Accumulation (SAMA) Strategy

4.1. Mechanism of the SAMA Strategy. The injected angular momentum by geomagnetic excitation is closely related to not only the Earth's magnetic intensity but also the SAMA. In the orbital coordinates $OX_oY_oZ_o$, the spacecraft-debris system can only accumulate angular momentum on the Y_o -axis or Z_o -axis in order to reach the required deorbiting velocity changes ΔV , as shown in Figure 4. And we hope that the angular momentum accumulation on the Y_o -axis or Z_o -axis can be maximized in a certain period of time; also, the accumulation on the other two axes can be minimized within one orbital period. Therefore, two SAMA strategies which correspond to the accumulation on the Y_o -axis and Z_o -axis are given, as shown in equations (10) and (11). Based on the strategies, we can adjust the direction or the magnitude of the magnetic moment carried by the delivery spacecraft in the entire angular momentum accumulation process.

$$\begin{cases} \text{Cmd}_m_x = \begin{cases} -\frac{2 \tan \varphi |\mathbf{m}|}{\sqrt{1+4 \tan^2 \varphi}} & -\frac{\pi}{2} \leq \varphi \leq \frac{\pi}{2}, \\ \frac{2 \tan \varphi |\mathbf{m}|}{\sqrt{1+4 \tan^2 \varphi}} & \frac{\pi}{2} \leq \varphi \leq \frac{3\pi}{2}, \end{cases} \\ \text{Cmd}_m_y = 0, \\ \text{Cmd}_m_z = \begin{cases} \frac{|\mathbf{m}|}{\sqrt{1+4 \tan^2 \varphi}} & -\frac{\pi}{2} \leq \varphi \leq \frac{\pi}{2}, \\ -\frac{|\mathbf{m}|}{\sqrt{1+4 \tan^2 \varphi}} & \frac{\pi}{2} \leq \varphi \leq \frac{3\pi}{2}, \end{cases} \end{cases} \quad (10)$$

$$\begin{cases} \text{Cmd}_m_x = 0, \\ \text{Cmd}_m_y = |\mathbf{m}|, \\ \text{Cmd}_m_z = 0, \end{cases} \quad (11)$$

where Cmd_m_x , Cmd_m_y , and Cmd_m_z are the expected component of the magnetic moment in the geomagnetic coordinates, $|\mathbf{m}|$ is the total magnetic moment that can be generated, and φ is the corresponding geographic latitude during on-orbit operation.

4.2. Deorbiting Capability under the SAMA Strategy. Based on the dipole model, substituting equations (2) and (3) into equation (8), we get

$$\begin{aligned} \mathbf{L}^o &= \mathbf{R}_{om} \cdot \mathbf{L}^m \\ &= \begin{bmatrix} (m_y B_z) \cdot \sin i \cdot \cos \kappa + (m_z B_x - m_x B_z) \cdot \sqrt{1 - \sin^2 i \cdot \cos^2 \kappa} \\ (m_z B_x - m_x B_z) \cdot \sin i \cdot \cos \kappa - (m_y B_z) \cdot \sqrt{1 - \sin^2 i \cdot \cos^2 \kappa} \\ (m_y B_x) \end{bmatrix}. \end{aligned} \quad (12)$$

Substituting equation (10) into equation (12) and supposing that the initial value of the corresponding geographic latitude is 0, the accumulation \mathbf{L}^o within one orbital period is given by equation (13) under strategy equation (10) (assuming that the system orbit is a circular orbit before deorbiting). By strategy equation (10), the magnetic torque in the Y_o -axis of orbital coordinates is always maximum and angular momentum can be gradually accumulated, while the magnetic torque in the X_o -axis and Z_o -axis, positive and negative, can wipe one another out in one orbital period and angular momentum accumulation is few (the accumulation is zero under the dipole model).

$$\begin{aligned} \int_0^{T_0} \mathbf{L}^o dt &= \begin{bmatrix} \int_0^{T_0} L_x^o dt \\ \int_0^{T_0} L_y^o dt \\ \int_0^{T_0} L_z^o dt \end{bmatrix} \\ &= \begin{bmatrix} \int_0^{T_0} (m_z B_x - m_x B_z) \cdot \sqrt{1 - \sin^2 i \cdot \cos^2 \kappa} dt \\ \int_0^{T_0} (m_z B_x - m_x B_z) \cdot \sin i \cdot \cos \kappa dt \\ \int_0^{T_0} 0 dt \end{bmatrix} \\ &= \begin{bmatrix} 0 \\ \frac{\mu_0 m_e |\mathbf{m}|}{\pi r^3} \int_0^{T_0/4} \sqrt{1 + 4 \tan^2 \varphi} \cdot \cos \varphi \cdot \sin i \cdot \cos \kappa dt \\ 0 \end{bmatrix}. \end{aligned} \quad (13)$$

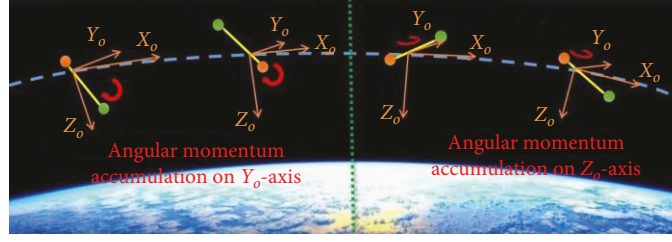


FIGURE 4: Diagram of angular momentum accumulation.

Also, substituting equation (11) into equation (12) and under strategy equation (11), the accumulation \mathbf{L}^o within one orbital period is given by equation (14) (assuming that the system orbit is a circular orbit before deorbiting). By strategy equation (11), the magnetic torque in the Z_o -axis of orbital coordinates is always maximum and angular momentum can be gradually accumulated, while the magnetic torque in the X_o -axis and Y_o -axis, positive and negative, can wipe one another out in one orbital period and angular momentum accumulation is few.

$$\begin{aligned}
 \int_0^{T_0} \mathbf{L}^o dt &= \begin{bmatrix} (m_y B_z) \cdot \sin i \cdot \cos \kappa \\ -(m_y B_z) \cdot \sqrt{1 - \sin^2 i \cdot \cos^2 \kappa} \\ (m_y B_x) \end{bmatrix} \\
 &= \begin{bmatrix} \frac{\mu_0 m_e |\mathbf{m}|}{2\pi r^3} \int_0^{T_0} \sin \varphi \cdot \sin i \cdot \cos \kappa dt \\ -\frac{\mu_0 m_e |\mathbf{m}|}{2\pi r^3} \int_0^{T_0} \sin \varphi \cdot \sqrt{1 - \sin^2 i \cdot \cos^2 \kappa} dt \\ \frac{\mu_0 m_e |\mathbf{m}|}{4\pi r^3} \int_0^{T_0} \cos \varphi dt \end{bmatrix} \\
 &= \begin{bmatrix} 0 \\ 0 \\ \frac{\mu_0 m_e |\mathbf{m}|}{4\pi r^3} \int_0^{T_0} \cos \varphi dt \end{bmatrix}.
 \end{aligned} \tag{14}$$

From equations (13) and (14) that we know, (i) under strategy equation (10), the angular momentum accumulation is in positive correlation with the inclination i ; when the inclination is small, the angular momentum accumulation within one orbital period is low (under the dipole model, the angular momentum accumulation is zero when the inclination is zero); (ii) under strategy equation (11), the longer the spacecraft stays in the low-latitude area, the higher the angular momentum accumulation is, which is more applicable to the small inclination orbit; and (iii) obviously, we can coordinate and adjust the above strategies to adapt to the condition of different inclinations.

Substituting equations (13) and (14) into equation (9), we obtain equations (15) and (16) (ceiling), respectively. From equations (15) and (16), when the altitude, space debris mass, length of delivery mechanism, and magnetic moment carried by the spacecraft are h , M_2 , R , and \mathbf{m} , respectively, and the set perigee altitude (i.e., ΔV) is sure, the space debris can meet the deorbiting condition within the N orbital period under strategy equation (10) or equation (11).

$$N \leq \frac{\pi(R_0 + h)^3 R \cdot M_2 \Delta V}{\mu_0 m_e |\mathbf{m}| \int_0^{T_0/4} \sqrt{1 + 4 \tan^2 \varphi \cdot \cos \varphi \cdot \sin i \cdot \cos \kappa} dt}, \tag{15}$$

$$N \leq \frac{\pi(R_0 + h)^3 R \cdot M_2 \Delta V}{\mu_0 m_e |\mathbf{m}| \int_0^{T_0/4} \cos \varphi dt}, \tag{16}$$

where R_0 denotes the Earth's radius and h denotes the orbital altitude of the delivery system.

5. Example Analysis

To verify the feasibility and performance of the proposed method for space debris deorbiting in the entire LEO regions, 9 simulation examples with a circular/elliptical orbit or different altitudes/inclinations are designed and analyzed, where examples from 1 to 5 are the simulation with the altitude below 1000 km and examples from 6 to 8 are the simulations with the altitude from 1000 km to 2000 km.

In examples, assume that the mass of the delivery spacecraft is 200 kg, the area-mass ratio is 0.003, the drag coefficient is 2.2, and the magnetic moment carried by the delivery spacecraft is 10^5 Am^2 (the level can be generated with existent technology). And set the right ascension of the ascending node, the argument of perigee, and true anomaly as equal to zero. The IGRF11 model is added for verification in examples. The dipole model distribution is taken as the principal component of the IGRF model, and the combination of the 13th-order spherical harmonics expression and the Gauss coefficient based on the measured data gives equation (17) of the IGRF model, where the 4th-order Runge-Kutta method is adopted to compute examples.

$$\begin{cases} B_x^I = \sum_{n=1}^{13} \sum_{m=0}^n \left(\frac{R_e}{r}\right)^{n+2} A_n^m \cdot \frac{dP_n^m(\cos \theta)}{d\theta} \times 10^{-9}, \\ B_y^I = \sum_{n=1}^{13} \sum_{m=0}^n \left(\frac{R_e}{r}\right)^{n+2} \frac{mB_n^m}{\sin \theta} \cdot P_n^m(\cos \theta) \times 10^{-9}, \\ B_z^I = -\sum_{n=1}^{13} \sum_{m=0}^n \left(\frac{R_e}{r}\right)^{n+2} (n+1)A_n^m \cdot P_n^m(\cos \theta) \times 10^{-9}, \end{cases} \quad (17)$$

where $A_n^m = g_n^m \cos(m\lambda) + h_n^m \sin(m\lambda)$, $B_n^m = g_n^m \sin(m\lambda) - h_n^m \cos(m\lambda)$, R_e is the Earth's radius, r is the geocentric distance, $\theta (= 90^\circ - \varphi')$ is the geocentric colatitude, φ' is the geocentric latitude, λ is the longitude, g_n^m and h_n^m are the Gauss coefficient changing with time, and $P_n^m(\cos \theta)$ is the first-order quadratic Legendre function. Based on the IGRF model, equation (10) can be written as equation (18), and in equation (18), the parameters of the IGRF model not the geographical latitude is used for the SAMA.

$$\begin{cases} \text{Cmd}_{m_x} = \begin{cases} -\frac{|\mathbf{m}| \cdot B_z^I}{\sqrt{(B_x^I)^2 + (B_y^I)^2 + (B_z^I)^2}} & -\frac{\pi}{2} \leq \varphi \leq \frac{\pi}{2}, \\ \frac{|\mathbf{m}| \cdot B_z^I}{\sqrt{(B_x^I)^2 + (B_y^I)^2 + (B_z^I)^2}} & \frac{\pi}{2} \leq \varphi \leq \frac{3\pi}{2}, \end{cases} \\ \text{Cmd}_{m_y} = 0, \\ \text{Cmd}_{m_z} = \begin{cases} \frac{|\mathbf{m}| \cdot B_x^I}{\sqrt{(B_x^I)^2 + (B_y^I)^2 + (B_z^I)^2}} & -\frac{\pi}{2} \leq \varphi \leq \frac{\pi}{2}, \\ -\frac{|\mathbf{m}| \cdot B_x^I}{\sqrt{(B_x^I)^2 + (B_y^I)^2 + (B_z^I)^2}} & \frac{\pi}{2} \leq \varphi \leq \frac{3\pi}{2}. \end{cases} \end{cases} \quad (18)$$

The atmospheric density is computed based on the NRLMSISE00 atmospheric model, and the weighted mean of atmospheric density changing with time and latitude and longitude in one year is taken as the average atmospheric density in the corresponding altitude, as shown in Table 3.

5.1. Example 1: Circular Orbit, Where Altitude and Inclination Are 950 km and 90°, Respectively, before Deorbiting. Under the dipole and IGRF11 model, strategy equations (10) and (18) accumulating angular momentum on the Y_o -axis of orbital coordinates are used to compute the magnetic torque and angular momentum accumulation, respectively, on the three axes in orbital coordinates. The results are shown in Figure 5, where dip-dip denotes the results using strategy equation (10) under the dipole model, dip-IGRF denotes the results using strategy equation (10) under the IGRF model, and IGRF-IGRF denotes the results

TABLE 3: Atmospheric annual mean density in different heights.

Altitude (km)	Atmospheric density (kg/m ³)
450	3.72×10^{-13}
550	6.08×10^{-14}
650	1.45×10^{-14}
750	5.45×10^{-15}
850	2.83×10^{-15}
950	1.72×10^{-15}

using strategy equation (18) under the IGRF model. From Figure 5, we know the following:

- (i) Results of dip-dip agree with equation (13), and the angular momentum is significantly accumulated only on the Y_o -axis of the orbit coordinates. With the 10^5 Am^2 level magnetic moment, the angular momentum accumulation can reach to nearly $1.7 \times 10^4 \text{ Nms}$ within one orbital period. Thus, the results show that the angular momentum accumulation in several days or less (several orbital periods) can meet the deorbiting requirement of 10 kg level LEO space debris
- (ii) The accumulation difference under the two models (dipole model and IGRF model) is about 10%, so the geomagnetic excitation deorbiting capability can be estimated by using equation (13)
- (iii) The magnetic axis of the dipole model is the Earth's rotational axis, while there are more than 10-degree angles between the actual magnetic axis of the Earth and its rotational axis, which makes the computing difference between the accumulation on the X_o -axis and Z_o -axis of orbital coordinates. Even so, the X_o -axis and Z_o -axis magnetic torque in orbital coordinates displays periodic, positive, and negative variations in one orbital period and the accumulated angular momentum after the positive and negative balance is less than the 2nd-order of Y_o -axis accumulation
- (iv) The computing results by using strategy equations (10) and (18) show no significant difference

5.2. Example 2: Circular Orbit, Where Inclination Is 90° before Deorbiting. At different circular orbit altitudes and based on the IGRF11 model, strategy equation (18) is used to compute the angular momentum accumulation on the three axes of orbital coordinates within one orbital period. Figure 6 shows the results, and the results show that the trend of the computing results is the same at different circular orbit altitudes by using strategy equation (18). The lower the altitude is, the greater the angular momentum accumulation is. The accumulated angular momentum changes at different altitudes mainly reflect the changes of the Earth's magnetic field intensity distribution with height.

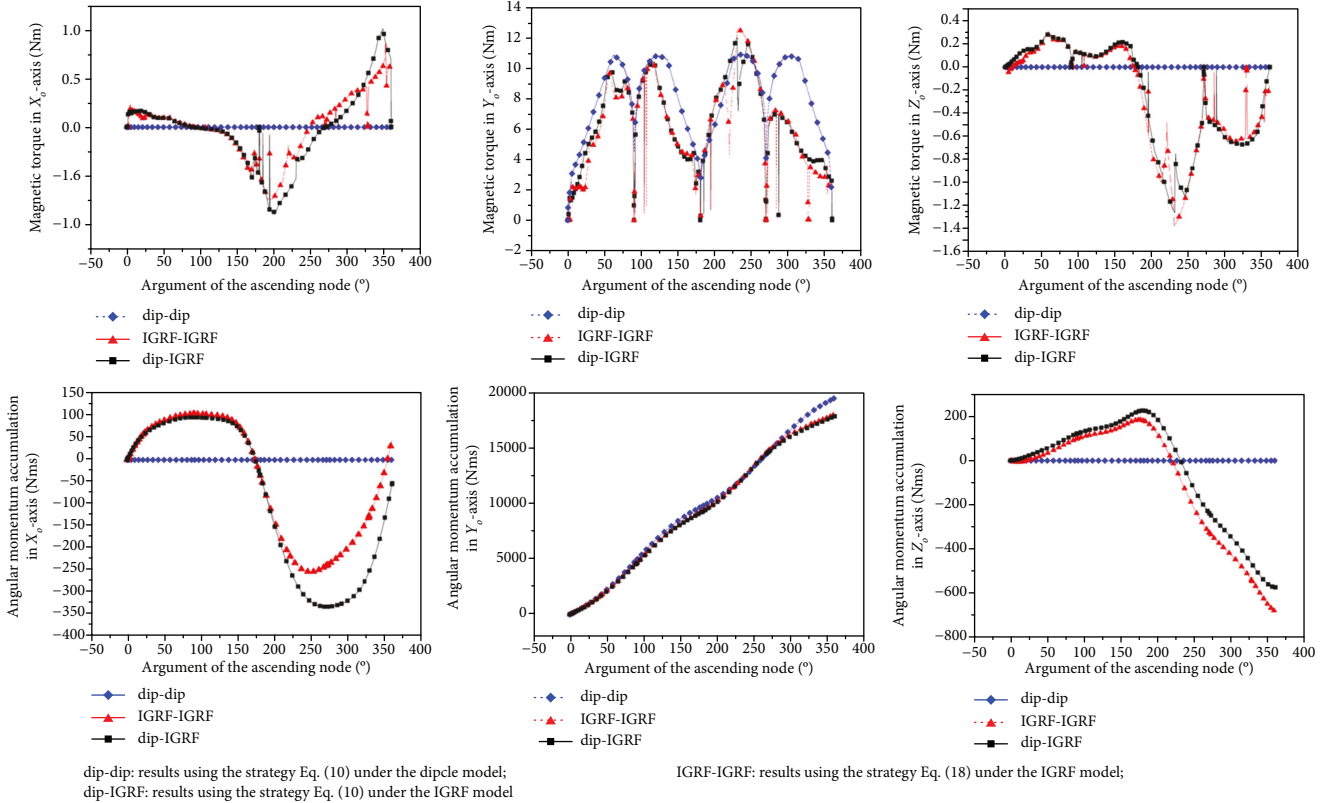


FIGURE 5: Magnetic torque and angular momentum accumulation (orbital coordinates) in the circular orbit (950 km) under equations (10) and (18) (example 1).

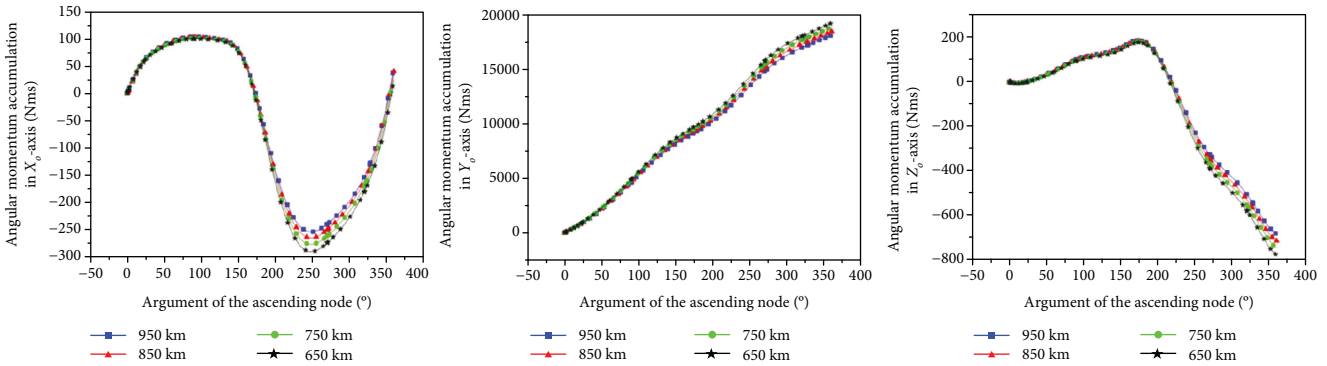


FIGURE 6: Magnetic momentum accumulation (orbital coordinates) in different circular orbit altitudes under equation (10) (example 2).

5.3. Example 3: Circular Orbit, Where Inclination Is Equal to 0° before Deorbiting. Under the dipole IGRF11 model, strategy equation (11)—accumulating the angular momentum on the Z_o-axis of orbital coordinates—is used to compute the magnetic torque and angular accumulation on the three axes in orbital coordinates. The results are shown in Figure 7. The results show that

(i) Strategy equation (11) can be used to the angular momentum accumulation on the Z_o-axis of orbital

coordinates, which is similar with the accumulation computation on the Y_o-axis of orbital coordinates. Also, under equation (11), the accumulation computing difference is small under the dipole model and IGRF11 model, which indicates that strategy equation (11) can be used for the deorbiting capability assessment of geomagnetic excitation

(ii) On the X_o-axis and Y_o-axis of orbital coordinates, the computing difference of the magnetic momentum accumulation is significantly different under the

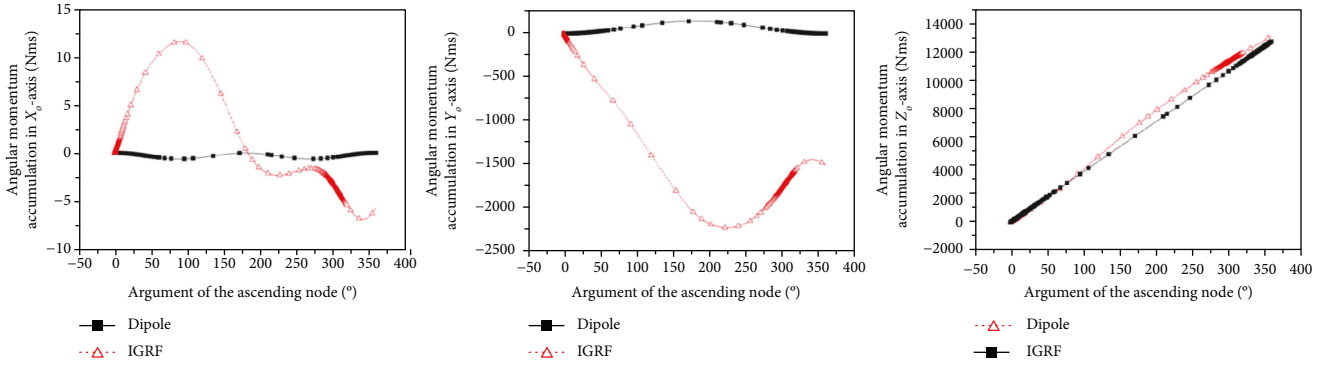


FIGURE 7: Angular momentum accumulation (orbital coordinates) in the circular orbit (950 km) by the dipole and IGRF11 model under equation (11) (example 3).

dipole and IGRF model, respectively. And under the IGRF model, the momentum accumulation on the Y_o -axis is a sixth of the accumulation in the principal direction (i.e., Z_o -axis)

5.4. Example 4: Elliptical Orbit, Where Perigee and Apogee Altitudes Are 300 km and 950 km, Respectively, and Inclinations Are Equal to 0° and 90° , Respectively, before Deorbiting. Under the dipole model, strategy equations (10) and (11) are used to compute the angular momentum accumulation on the Y_o -axis and Z_o -axis, respectively, of orbital coordinates. The results are shown in Figure 8. Comparing the two in Figure 8, using the accumulation strategy on the Y_o -axis of orbital coordinates will sharply weaken the accumulated capability of the deorbiting system in the small inclination orbit, while using the accumulation strategy on the Y_o -axis can make the system in the large inclination orbit gain the same level of accumulated capability of the system in the small inclination orbit.

5.5. Example 5: Circular Orbit, Where Altitude Is 950 km and Inclination Is Different before Deorbiting. Based on the IGRF11 model and under the different circular orbit, strategy equations (11) and (18) are, respectively, used to compute the angular momentum accumulation on the three axes of orbital coordinates within one orbital period. Figure 9 shows the results, and the results show that

- (i) By using the SAMA strategy on the Y_o -axis of orbital coordinates, the accumulated capability decreases rapidly with the decrease of the inclination, while by using the accumulation strategy on the Z_o -axis, the accumulated capability decreases with the increase of the inclination, but without changes in order
- (ii) With changes in inclination, using accumulation strategy equation (18) on the Y_o -axis of orbital coordinates or equation (11) on the Z_o -axis will cause the accumulation peak with large amplitude on the X_o -axis and Y_o -axis, where the angular momentum can be accumulated on the X_o -axis of orbital coordinates by using strategy equation (18), while using equation (11), the angular momentum is alternately

accumulated on the X_o -axis and Y_o -axis of orbital coordinates

5.6. Example 6: Circular Orbit, Where Altitude and Inclination Are 1950 km and 90° , Respectively, before Deorbiting. Similar to previous example 1, strategy equations (10) and (18) are used to compute the magnetic torque and angular momentum accumulation, respectively, under the dipole and IGRF model. Figure 10 shows the results, and the results show that

- (i) Only results of dip-dip under the dipole model agree with equation (13), and the angular momentum is accumulated only on the Y_o -axis of the orbit coordinates, which is the same with conclusion (i) of example 1 in Section 5.1 and has the same deorbiting capability with it
- (ii) Results of dip-IGRF and IGRF-IGRF under the IGRF model are abnormal along with the increase of the argument of the ascending node, which can be confirmed by Ref. [54]

In Ref. [54], the measured data-based IGRF model is used to predict the Earth's main internal magnetic field vector and Matteo and Morton confirmed that by the comparison of prediction by the IGRF model and satellite measurements, the IGRF model remains highly accurate in the LEO below 1000 km, even in geomagnetically active conditions. The geomagnetic field extends far out into the space, but because of the influence of solar wind and others, the IGRF model is not valid in the LEO above 1000 km, especially that near 2000 km, leading to the abnormal results in conclusion (ii). Therefore, the effectiveness of the proposed SAMA strategies is verified only under the dipole model in the following examples.

5.7. Example 7: Circular Orbit, Where Altitude/Inclination Is Different before Deorbiting. Under the dipole model, angular momentum accumulation is computed only under strategy equation (10) in this example. Given the length limitations, only results of angular momentum accumulation are shown in Figures 11 and 12 and show that either strategy equation (10) or strategy equation (11) yields the same results with

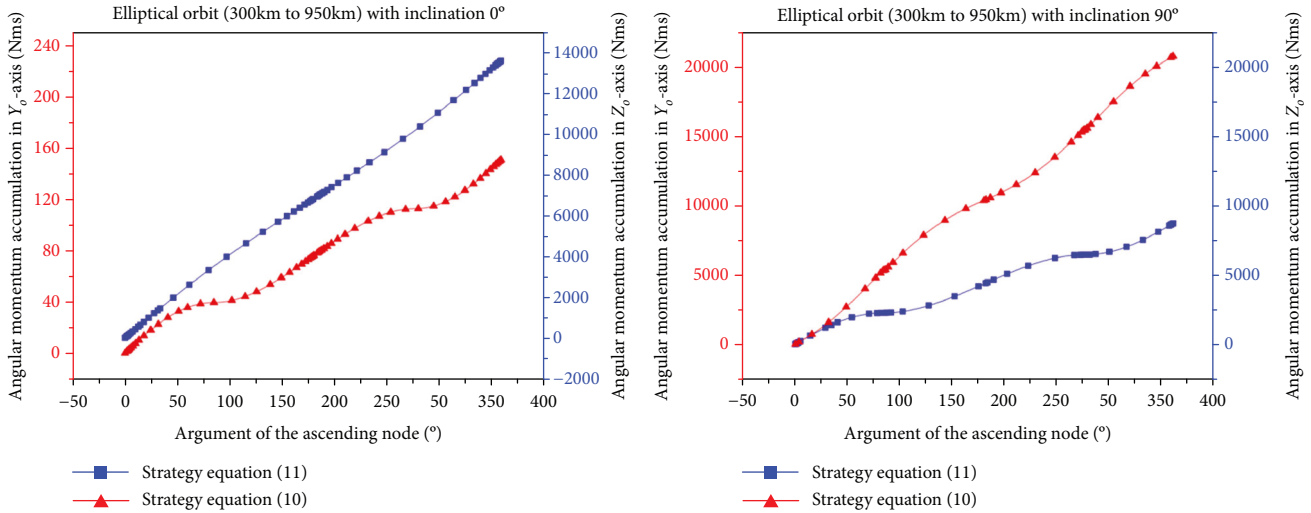


FIGURE 8: Main angular momentum accumulation (orbital coordinates) in the elliptical orbit with an inclination of $0^\circ/90^\circ$ (300 km to 950 km) under equations (11) and (10) (example 4).

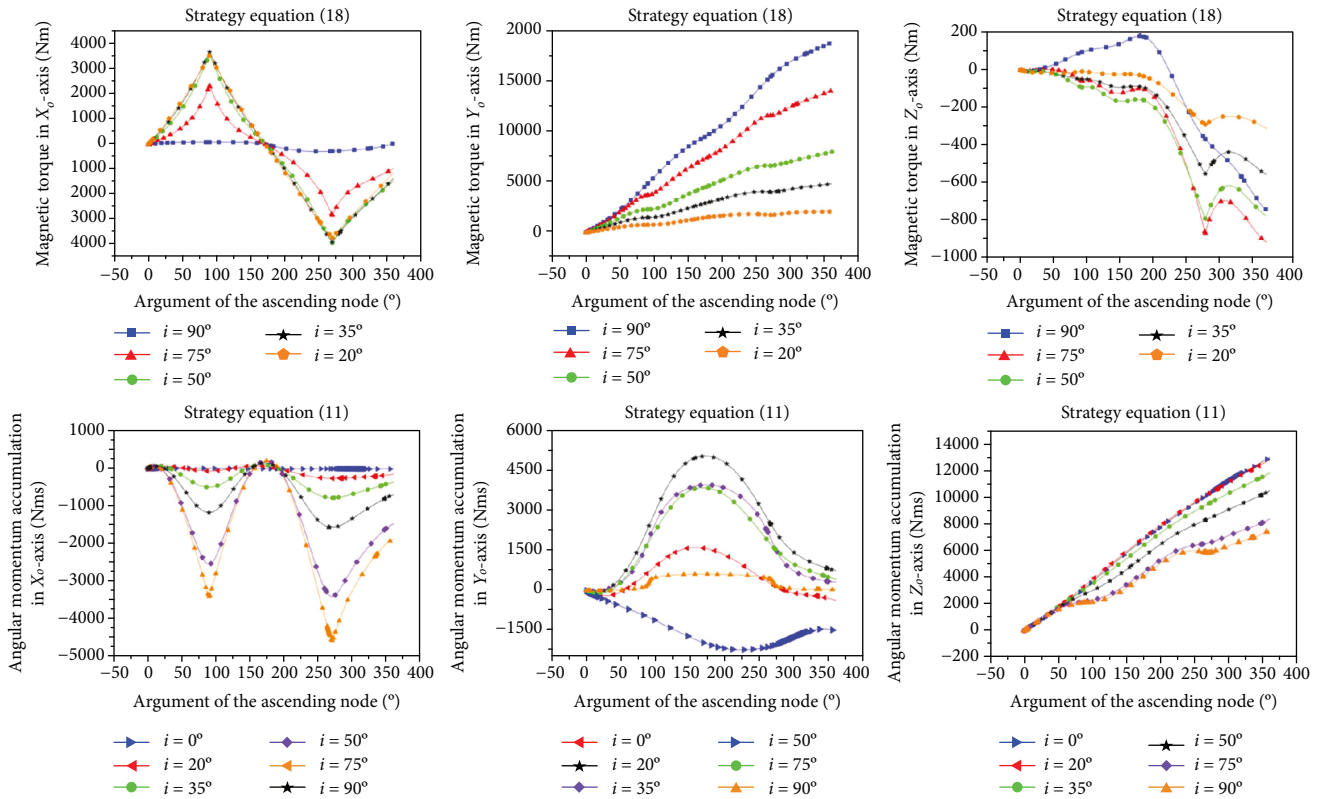


FIGURE 9: Angular momentum accumulation (orbital coordinates) in different inclination circular orbits (950 km) under equations (11) and (18) (example 5).

those of example 2 in Section 5.2 or those of example 5 in Section 5.5, respectively.

5.8. Example 8: Elliptical Orbit, Where Perigee and Apogee Altitudes Are 400 km and 1950 km, Respectively, and Inclination is Equal to 90° before Deorbiting. Also, angular momentum accumulation in the elliptical orbit is analyzed under the dipole and IGRF model. Due to the space

limitations, we only give the angular momentum accumulation under strategy equation (10), shown in Figure 13. Results indicate that

- (i) Only results of dip-dip under the dipole model agree with equation (13), and the angular momentum is accumulated only on the Y_o -axis of the orbit coordinates, which is the same with the conclusion of

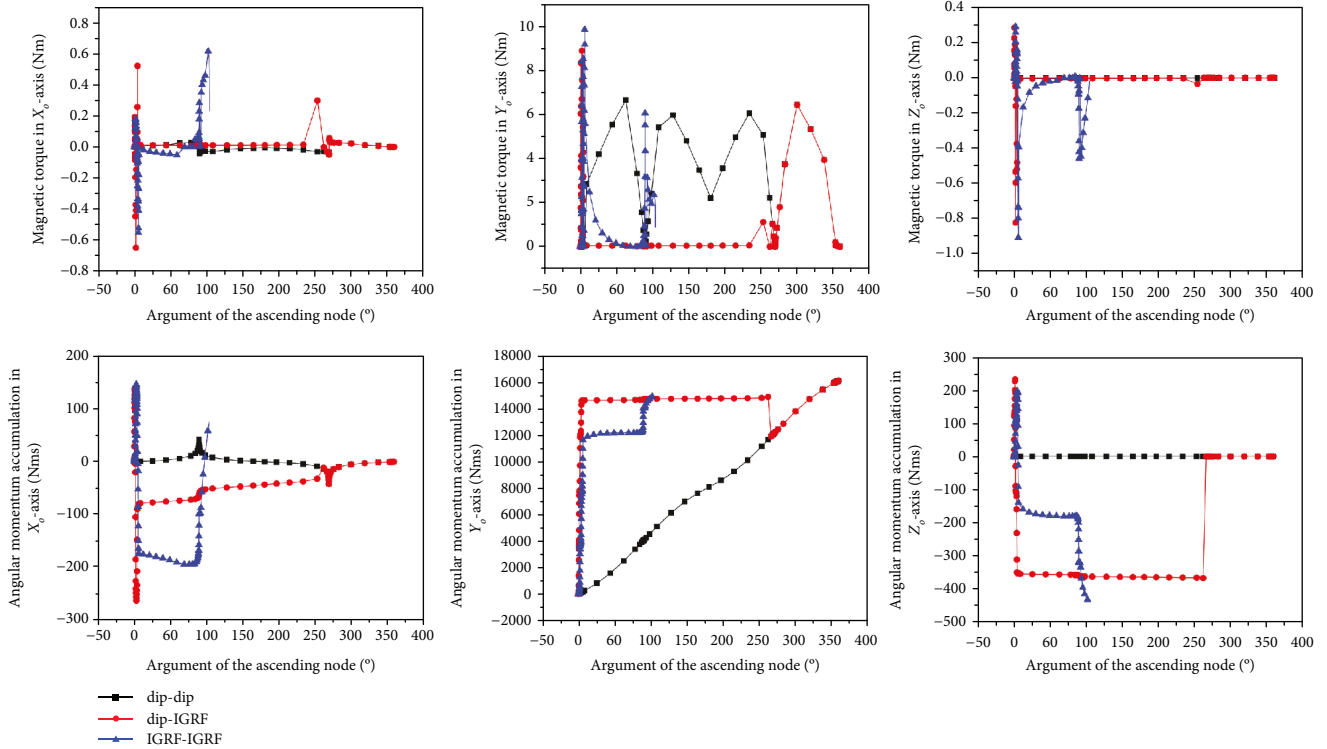


FIGURE 10: Magnetic torque and angular momentum accumulation (orbital coordinates) in the circular orbit (1950 km) under equations (10) and (18) (example 6).

example 4 in Section 5.4 and has the same deorbiting capability with it

- (ii) Along with the increase of the argument of the ascending node, the angular momentum on the three axes of dip-IGRF and IGRF-IGRF under the IGRF model no longer continues to increase when the argument of the ascending node is equal to about 175° . The reason why is that the altitude is over 1000 km, which can be confirmed by Ref. [54]

5.9. Summary. From comprehensive analysis of the 8 examples above, it is seen that

- (i) The validity of SAMA strategy equations (10), (11), and (18) and the correctness of magnetic torque accumulation estimation equations (13) and (14) are illustrated
- (ii) The computing results demonstrate the basic capability of using geomagnetic excitation to achieve LEO space debris deorbiting

So, we define $R \cdot M_2/|\mathbf{m}|$ as the characteristic coefficient of the spacecraft-debris system, which can characterize the LEO space debris deorbiting capability under any inclination i and in a certain deorbiting orbital period N required. The larger the value of $R \cdot M_2/|\mathbf{m}|$ is, the stronger is the debris deorbiting capability. With equations (15) and (16), we further carry out the deorbiting capability example 9 within

different deorbiting orbital periods N required, as shown in Figure 14.

In Figure 14, under strategy equations (10) and (11), the solid line and dashed line are the results of $R \cdot M_2/|\mathbf{m}|$ of altitude $h = 700 \text{ km}$; when $N = 30$, the plus direction of the error bar is the result of $R \cdot M_2/|\mathbf{m}|$ from $h = 700 \text{ km}$ to $h = 500 \text{ km}$ and the minus direction is the result of $R \cdot M_2/|\mathbf{m}|$ from $h = 700 \text{ km}$ to $h = 900 \text{ km}$. From Figure 14 and combined with the above example results, we know that

- (iii) The accumulation strategy on the Y_o -axis of orbital coordinates (i.e., equation (10) or equation (18)) has an obvious advantage in the large inclination orbit ($i > 49.16^\circ$, such as the Sun-synchronous orbit). Figure 15(a) is the deorbiting capability of strategy equation (10) under large inclination when $|\mathbf{m}| = 10^5 \text{ Am}^2$
- (iv) Besides the advantage in the small inclination ($i < 49.16^\circ$), the accumulation strategy on the Z_o -axis (i.e., equation (11)) can make the spacecraft-debris system in the LEO with different inclinations get stable angular momentum accumulation. And the strategy is extremely simple. Figure 15(b) is the deorbiting capability of strategy equation (11) under small inclination when $|\mathbf{m}| = 10^5 \text{ Am}^2$
- (v) If the altitude is less than 1000 km, the proposed SAME method by geomagnetic excitation can be applied to the entire regions with different

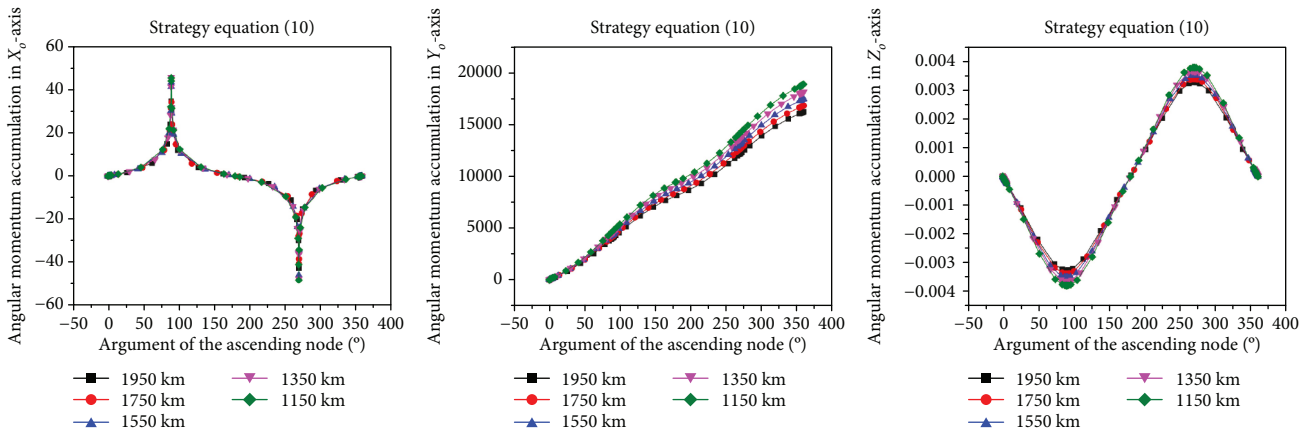


FIGURE 11: Angular momentum accumulation in the circular orbit (90°) with different altitudes under equation (10) (example 7).

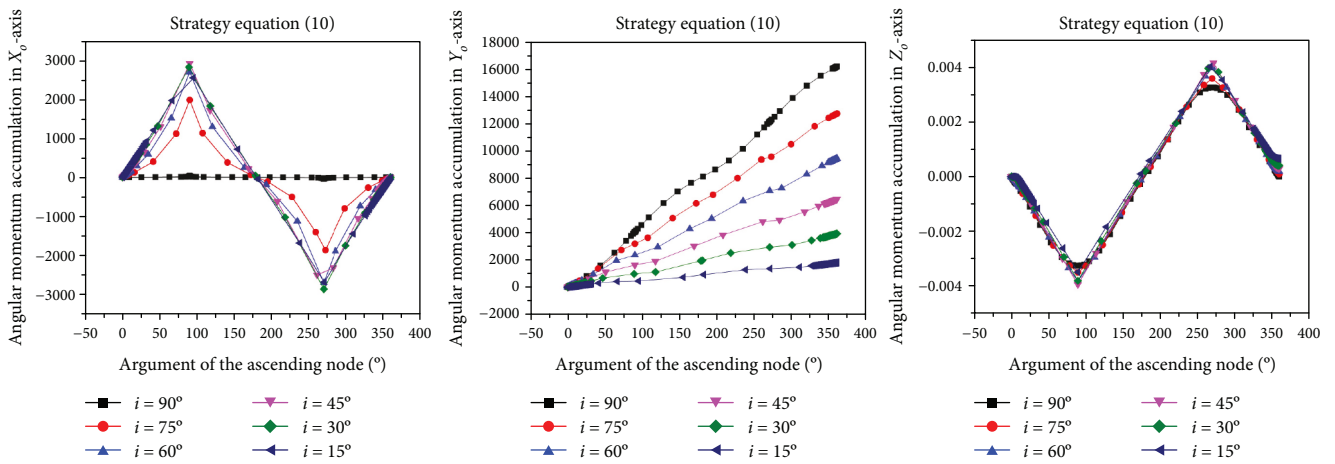


FIGURE 12: Angular momentum accumulation in the circular orbit (1950 km) with different inclinations under equation (10) (example 7).

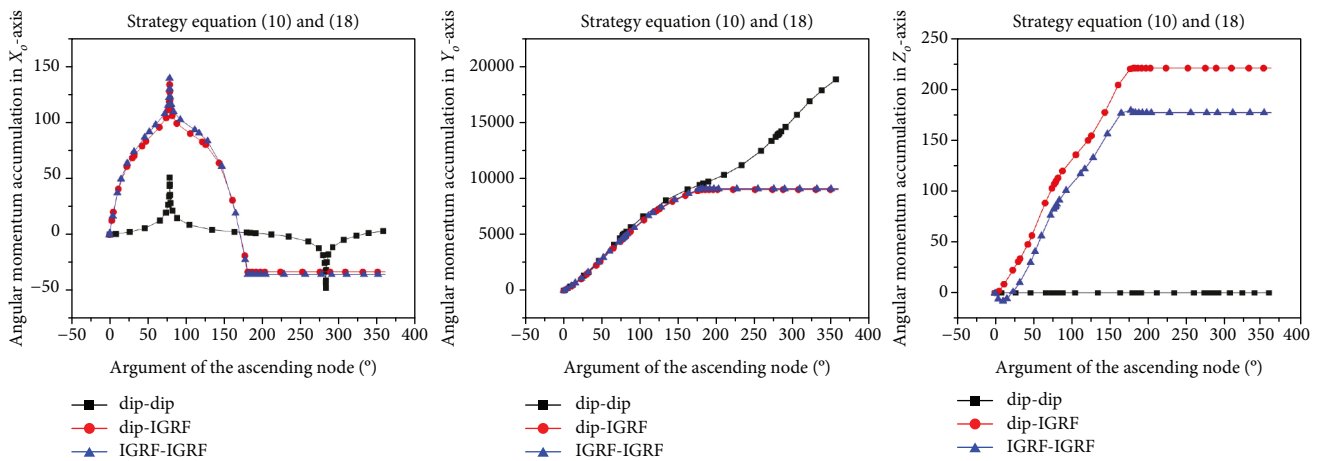


FIGURE 13: Main angular momentum accumulation (orbital coordinates) in the elliptical orbit with an inclination of 90° (400 km to 1950 km) under equation (10) (Example 8).

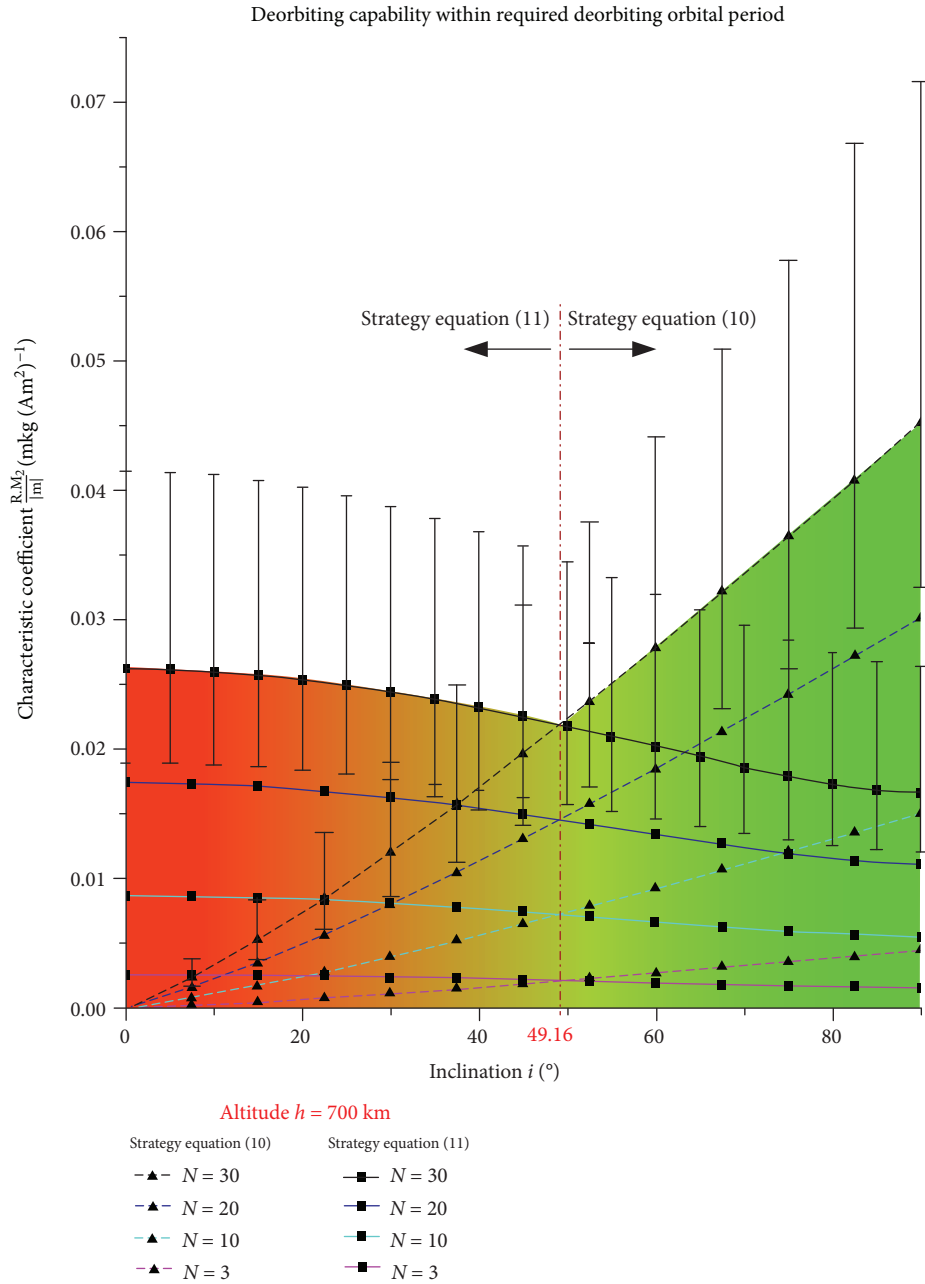


FIGURE 14: Deorbiting capability within different deorbiting orbital periods N required (example 9).

altitudes/inclinations and eccentricities; with the 10^5 Am² level magnetic moment, only several days of preparation is required for about 10^4 m·kg mechanism-scale-debris-mass deorbiting, seen in Figure 15. For the LEO above 1000 km, the dipole model-based SAMA strategy has almost the same deorbiting capability with that for the LEO below 1000 km; however, considering that the actual geo-magnetic field distribution is affected by solar wind and other effects [54], the improved study of SAMA strategies needs to be further completed in the future.

6. Key Technology for the Proposed Deorbiting Method

As analyzed above, the proposed method is theoretically feasible for LEO space debris deorbiting and has outstanding advantage over the exiting space debris methods in many aspects, including economy, safety, and maneuverability. But a breakthrough is still necessary in some key technologies from theoretical foundation to practical realization.

6.1. Angular Momentum Accumulation and Space Debris Deorbiting Planning Technology. The two SAMA strategies

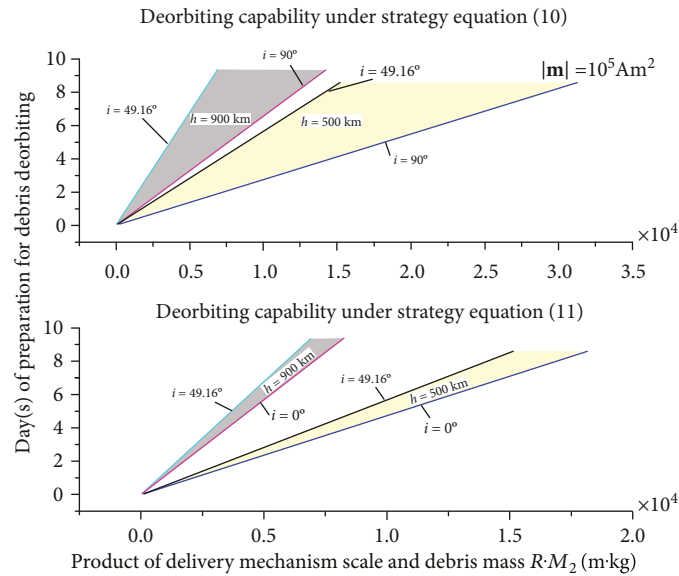


FIGURE 15: Deorbiting capability under strategy equations (10) and (11).

are proposed in this paper, and obviously, they can be further optimized and improved. Taking the results of example 1 (i.e., Figure 5) as an example, when the argument of the ascending node is about 0° or 90° , the magnetic torque in the Y_o -axis of orbital coordinates is small and the magnetic torque in the X_o -axis is larger. So, with this distribution feature of the geomagnetic field, the entire period can be divided into two parts: working period and adjustment period, as shown in Figure 16. By the way of accumulating angular momentum in the working period and unloading angular momentum of the other directions or storing kinetic/electric energy in the adjustment period, the geomagnetic field can be well utilized to simultaneously realize the accumulation of the angular momentum and elimination of the additional angular momentum. Under the premise of achieving the required deorbiting velocity, it is flexible to choose the debris deorbiting time and orientation angle. With this loose deorbiting constraint condition, other strategies and methods need to be further studied except the above simple improvement, including the combination of the two proposed strategies, the angular accumulation strategy in the high Earth orbit (orbital altitude ≥ 1000 km), and the flexible deorbiting strategy and method.

The exchanged momentum generated by space debris deorbiting can be used for the orbit transfer and maneuver of the delivery spacecraft (such as moving toward the next space debris to be deorbited), so the corresponding deorbiting planning is also an important application in the future.

6.2. Delivery Mechanism Design Technology. The delivery mechanism of geomagnetic excitation is the actuator for the implementation of the proposed method. In addition to complete the generation, maintenance, and adjustment of the strong magnet, the delivery mechanism with high integration and reliability also connects the delivery spacecraft and the space debris to be deorbited to complete the

magnetic-torque-to-angular momentum exchange and eliminate the effect of the coupled magnetic torque.

Taking the deorbiting in the 900 km circular orbit as an example, the required velocity change for the space debris deorbiting is 200 m/s. When the distance from the space debris to the system centroid is 10 m, the centrifugal overload exerted on the delivery mechanism can reach 400 g, which puts forward higher requirement to the connection, momentum exchange, and deorbiting package. Hence, this will certainly require us to increase the scale; when the scale reaches the 100 m level, the centrifugal overload will be reduced to 40 g. The scale of the delivery mechanism is much less than the electrodynamic tether's, but there are still many challenges in the delivery mechanism design.

6.3. Geomagnetic Excitation Delivery Dynamics and Control Technology. By the angular momentum injection capability, the effectiveness of the LEO space debris deorbiting by geomagnetic excitation is preliminarily evaluated. Obviously, the delivery effectiveness by geomagnetic excitation is closely related to the delivery control method and delivery mechanism design. In the process of angular momentum injection by geomagnetic excitation, the dynamics and trajectory of the spin body under active control of the magnet are obviously in strong coupling with the spacecraft orbit; besides, the entire spin system under the perturbation and active control force has the nutation property. So, using the flexible connection (such as tether), the system scale can be greatly increased and flexible to change, which will bring a lot of problems of geomagnetic excitation delivery dynamics and complex system control.

6.4. Gyroscopic Effect Analysis and Dynamics Modeling Technology. We make several strong assumptions when studying deorbiting capability estimation in Section 3.3, including rigid and massless connection (can be a tether) between debris and delivery spacecraft and no consideration

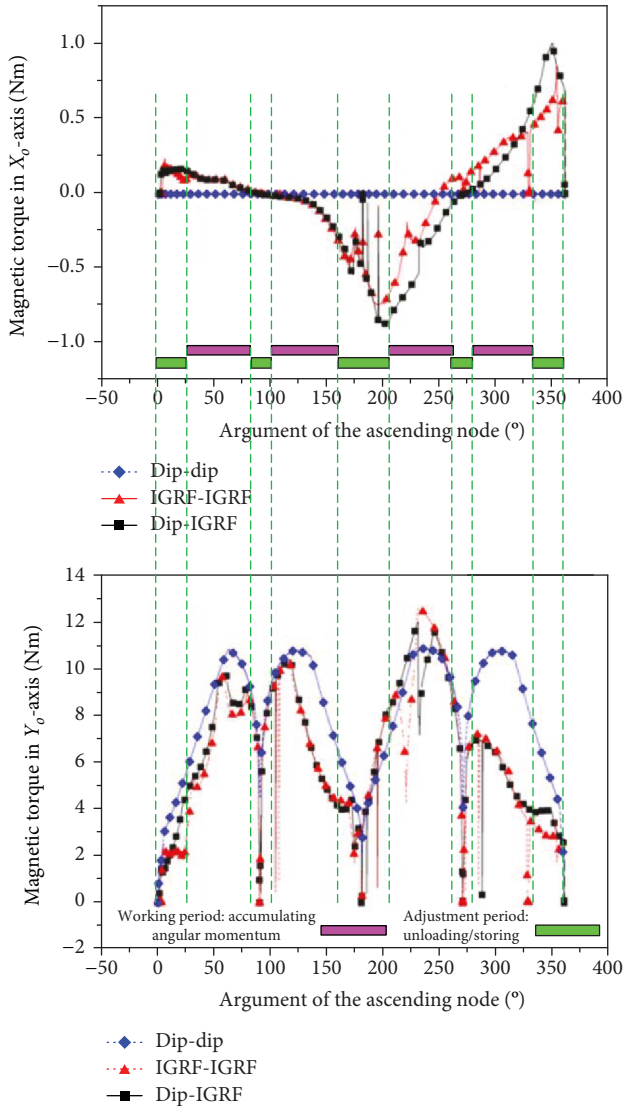


FIGURE 16: Diagram of a simple programming SAMA strategy.

for gyroscopic effect. As the main rotating unit of the SAME system, delivery mechanism at high spin speed will be subjected to centrifugal force effect and gyroscopic moment effect, so that the dynamics characteristics of the spacecraft-debris system change greatly compared with those of the static state. Therefore, the dynamics characteristic analysis and reliable and accurate dynamics modeling of the system are indispensable to efficient LEO debris deorbiting.

7. Conclusion and Prospect

First, the paper proposes a new method for LEO space debris deorbiting by geomagnetic excitation. The proposed method does not require the working medium consumption and not have the upper limit of the angular momentum injection; besides, the effectiveness of SAME relies primarily on the magnitude of the angular momentum; thus, it greatly reduces the scale requirement, which can successfully avoid the collision risk of the large-scale spacecraft in the orbit.

Compared with the tether's momentum exchange using altitude difference, the SAME can be more flexible in the application of the orbit transfer out of the orbital plane and the mixed orbit transfer both in and out of the orbital plane. So, the application of the proposed method is not limited to space debris deorbiting. Imagine that the method is applied to a space-based delivery platform in the orbit, as the relay station of tripping from the space to Earth. Through the platform, the spacecraft is accelerated and then delivered to the desired orbit, while the reentry capsule is decelerated and then delivered to the reentry corridor. We even can further establish a large-scale and low-cost space delivery network, greatly facilitating the development and utilization of space resources for human beings. And the flexible delivery capability and the reaction kinetic energy after delivery have great potential for space travel.

Second, the paper presents two SAMA strategies for LEO delivery; besides, under the two models of dipole and IGRF11, the angular momentum accumulation capability is evaluated. The results show that with the 10^5 Am^2 level magnetic moment, the SAMA can reach to at least the 10^4 level Nms within one orbital period in the LEO below 1000 km with any inclination; only several days of preparation is required for about $10^4 \text{ m}\cdot\text{kg}$ mechanism-scale-debris-mass deorbiting. And each of the two proposed strategies has its own characteristics; the SAMA strategy on the Z_o -axis (i.e., equation (11)) is extremely simple so that the two strategies can be mixed and be time sharing planned in the entire accumulation process. Obviously, the SAMA strategies by geomagnetic excitation still have the further optimizing space.

Third, the example results show that the proposed SAME method by geomagnetic excitation can be applied to the entire regions of the LEO below 1000 km with different altitudes/inclinations and eccentricities. When the altitude is more than 1000 km, the geomagnetic field may be disturbed by external factors such as solar wind. So, it is not clear whether the proposed method is useful for the higher-altitude (more than 1000 km) orbit and the corresponding SAMA strategy needs to be further studied. Under the two models of dipole and IGRF11, the computing results by the proposed SAMA strategy show no significant difference; thus, in the SAMA control of actual flight, we can use the simpler preinstallation programs, saving the trouble of measuring the Earth's magnetic field in the flying position at all times.

Finally, the paper gives the prospects of the required key technologies for LEO delivery and deorbiting by geomagnetic excitation. The proposed method has many problems to be further studied, including the scientific mechanism, technical challenge, and engineering implementation. With the existing technology and its development trend, the generation technology of small-scale low-power controlled strong magnet, the on-orbit approaching and capturing technology, and the angular momentum management and control technology have been basically overcome; based on the objective physical environment of the LEO magnetic field and the above estimation results, the proposed deorbiting strategy by geomagnetic excitation is physically feasible and there is almost no technology problem that cannot be solved.

Compared with the existing methods [10], it has the characteristics of no working medium consumption, rapid deorbiting, high flexibility, and low dependence on the scale and enjoys a broad prospect of application in LEO space in the future.

Data Availability

The data of the required deorbiting velocity changes and the atmospheric annual mean density in different heights used to support the findings of this study are included within the article; the data of the International Geomagnetic Reference Field (IGRF11) model used to support the findings of this study are available at the official website of the National Oceanic and Atmospheric Administration (NOAA) (<https://www.ngdc.noaa.gov>).

Conflicts of Interest

The authors declare that they have no conflicts of interest.

Acknowledgments

This study is supported by the Strategic Priority Research Program of the Chinese Academy of Sciences (Grant no. XDA17030200), National Natural Science Foundation of China (Grant nos. 11702294 and 11002143), and Key Project of Chinese National Programs for Fundamental Research and Development, 973 Program (Grant no. 2013CB733000).

Supplementary Materials

Supplementary Table 1: deorbiting capability within the required deorbiting orbital period. (*Supplementary Materials*)

References

- [1] P. Huang, L. Chen, B. Zhang, Z. Meng, and Z. Liu, "Autonomous rendezvous and docking with nonfull field of view for tethered space robot," *International Journal of Aerospace Engineering*, vol. 2017, Article ID 3162349, 11 pages, 2017.
- [2] G. Li, Z. H. Zhu, and S. A. Meguid, "Libration and transverse dynamic stability control of flexible bare electrodynamic tether systems in satellite deorbit," *Aerospace Science and Technology*, vol. 49, pp. 112–129, 2016.
- [3] D. J. Kessler and B. G. Cour-Palais, "Collision frequency of artificial satellites: the creation of a debris belt," *Journal of Geophysical Research*, vol. 83, no. A6, pp. 2637–2646, 1978.
- [4] T. Kelso, "Satcat boxscore," <https://celestrak.com/satcat/boxscore.php>.
- [5] J. C. Liou, "An active debris removal parametric study for leo environment remediation," *Advances in Space Research*, vol. 47, no. 11, pp. 1865–1876, 2011.
- [6] "Active debris removal," http://www.esa.int/Our_Activities/Operations/Space_Debris/Active_debris_removal.
- [7] M. Roddy, H. Hodges, L. Roe, and P.-H. A. Huang, "Demonstration of a solid-state inflation balloon deorbiter," in *ASME 2017 International Mechanical Engineering Congress and Exposition, Vol. 10*, pp. 1–6, Tampa, FL, USA, 2017.
- [8] J. Silva Neto, D. Sanchez, A. Prado, and G. Smirnov, "On the use of controlled radiation pressure to send a satellite to a graveyard orbit," *Revista Mexicana de Astronomia y Astrofisica*, vol. 53, pp. 321–332, 2017.
- [9] B. Patel, K. Kaurase, and P. Mishra, "A critical review on safe disposal techniques of space debris," *Journal of Geography, Environment and Earth Science International*, vol. 12, no. 3, pp. 1–6, 2017.
- [10] M. Shan, J. Guo, and E. Gill, "Review and comparison of active space debris capturing and removal methods," *Progress in Aerospace Sciences*, vol. 80, pp. 18–32, 2016.
- [11] Y. Zhao, P. Huang, and F. Zhang, "Dynamic modeling and super-twisting sliding mode control for tethered space robot," *Acta Astronautica*, vol. 143, pp. 310–321, 2018.
- [12] Y. Liu, P. Huang, F. Zhang, and Y. Zhao, "Robust distributed consensus for deployment of tethered space net robot," *Aerospace Science and Technology*, vol. 77, pp. 524–533, 2018.
- [13] M. L. Cosmo and E. C. Lorenzini, *Tethers in Space Handbook*, 1997.
- [14] "e.Deorbit," https://www.esa.int/Our_Activities/Space_Engineering_Technology/Clean_Space/e.Deorbit.
- [15] W. Gołębowski, R. Michalczyk, M. Dyrek, U. Battista, and K. Wormnes, "Validated simulator for space debris removal with nets and other flexible tethers applications," *Acta Astronautica*, vol. 129, pp. 229–240, 2016.
- [16] J. Zhang, K. Yang, and R. Qi, "Dynamics and offset control of tethered spacetug system," *Acta Astronautica*, vol. 142, pp. 232–252, 2018.
- [17] F. Zhang, P. Huang, Z. Meng, Y. Zhang, and Z. Liu, "Dynamics analysis and controller design for maneuverable tethered space net robot," *Journal of Guidance, Control, and Dynamics*, vol. 40, no. 11, pp. 2828–2843, 2017.
- [18] J. Reed and S. Barraclough, "Development of harpoon system for capturing space debris," in *6th European Conference on Space Debris*, pp. 1–8, Darmstadt, Germany, 2013.
- [19] R. Dudziak, S. Tuttle, and S. Barraclough, "Harpoon technology development for the active removal of space debris," *Advances in Space Research*, vol. 56, no. 3, pp. 509–527, 2015.
- [20] M. A. Amiri Atashgah, H. Gazerpour, A. Lavaei, and Y. Zarei, "An active timeoptimal control for space debris deorbiting via geomagnetic field," *Celestial Mechanics and Dynamical Astronomy*, vol. 128, no. 2-3, pp. 343–360, 2017.
- [21] H. Hakima and M. R. Emami, "Assessment of active methods for removal of leo debris," *Acta Astronautica*, vol. 144, pp. 225–243, 2018.
- [22] G. Sánchez-Arriaga, J. R. Sanmartín, and E. C. Lorenzini, "Comparison of technologies for deorbiting spacecraft from low-earth-orbit at end of mission," *Acta Astronautica*, vol. 138, pp. 536–542, 2017.
- [23] M. Dobrowolny and N. H. Stone, "A technical overview of tss-1: the first tethered-satellite system mission," *Il Nuovo Cimento C*, vol. 17, no. 1, pp. 1–12, 1994.
- [24] J. A. Carroll and J. C. Oldson, "Tethers for small satellite applications," in *1995 AIAA/USU Small Satellite Conference*, pp. 1–16, Logan, UT, USA, 1995.
- [25] D. P. Stern and M. Peredo, "The space tether experiment," <https://www-istp.gsfc.nasa.gov/Education/wtether.html>.
- [26] B. S. Yu, H. Wen, and D. P. Jin, "Review of deployment technology for tethered satellite systems," *Acta Mechanica Sinica*, vol. 34, no. 4, pp. 754–768, 2018.
- [27] H. Wen, D. Jin, and H. Hu, "Removing singularity of orientation description for modeling and controlling an

- electrodynamic tether,” *Journal of Guidance, Control, and Dynamics*, vol. 41, no. 3, pp. 764–769, 2018.
- [28] G. Li and Z. H. Zhu, “Parameter influence on electron collection efficiency of a bare electrodynamic tether,” *Science China Information Sciences*, vol. 61, no. 2, 2018.
- [29] G. Li and Z. H. Zhu, “Precise analysis of deorbiting by electrodynamic tethers using coupled multiphysics finite elements,” *Journal of Guidance, Control, and Dynamics*, vol. 40, no. 12, pp. 3348–3357, 2017.
- [30] N. Qi, Y. Yang, J. Zhao, Q. Sun, and W. Zhang, “Effects of asymmetries on the dynamics of motorized momentum exchange tether and payloads injection precision,” *International Journal of Aerospace Engineering*, vol. 2015, Article ID 468482, 13 pages, 2015.
- [31] V. S. Aslanov and A. S. Ledkov, “Swing principle in tether-assisted return mission from an elliptical orbit,” *Aerospace Science and Technology*, vol. 71, pp. 156–162, 2017.
- [32] G. V. Khazanov, E. N. Krivorutsky, and D. L. Gallagher, “Electrodynamic bare tether systems as a thruster for the momentum-exchange/electrodynamic reboost (MXER) project,” *Journal of Geophysical Research: Space Physics*, vol. 111, no. A4, pp. 251–257, 2006.
- [33] J. Bonometti, K. Sorensen, J. Dankanich, and K. Frame, “2006 status of the momentum exchange electrodynamic re-boost (MXER) tether development,” in *42nd AIAA/ASME/SAE/ASEE Joint Propulsion Conference & Exhibit*, pp. 1–15, Sacramento, CA, USA, 2013.
- [34] H. Yu, H. Li, Y. Wang, L. Cui, S. Liu, and J. Yang, “Brief review on pulse laser propulsion,” *Optics & Laser Technology*, vol. 100, pp. 57–74, 2018.
- [35] P. Tadini, U. Tancredi, M. Grassi et al., “Comparison of chemical propulsion solutions for large space debris active removal,” in *Chemical Rocket Propulsion*, Springer, 2017.
- [36] W. D. Deininger, M. Kendall, S. Enger et al., “Modular solar electric propulsion (SEP) tug concept,” in *2016 IEEE Aerospace Conference*, pp. 1–12, Big Sky, MT, USA, 2016.
- [37] A. Ruggiero, P. Pergola, and M. Andrenucci, “Small electric propulsion platform for active space debris removal,” *IEEE Transactions on Plasma Science*, vol. 43, no. 12, pp. 4200–4209, 2015.
- [38] “Electric versus chemical propulsion,” <http://sci.esa.int/smart-1/34201-electric-spacecraft-propulsion/?fbbodylongid=1535>.
- [39] D. Estublier, G. Saccoccia, and G. D. A. Jose, “Electric propulsion on smart-1 a technology milestone,” *ESA Bulletin*, vol. 129, pp. 40–46, 2007.
- [40] D. Reintsema, J. Thaeter, A. Rathke, W. Naumann, P. Rank, and J. Sommer, “Deos – the german robotics approach to secure and de-orbit malfunctioned satellites from low earth orbits,” in *i-SAIRAS 2010*, pp. 244–251, Sapporo, Japan, 2010.
- [41] J. Liu, Q. Huang, T. Yang, X. Chen, and Y. Wang, “Whole-body compliance for multi-arm space robotic capturing of large tumbling target in connection compliant phase,” *Advances in Mechanical Engineering*, vol. 10, no. 4, 2018.
- [42] X. Zhang and J. Liu, “Autonomous trajectory planner for space telerobots capturing space debris under the teleprogramming framework,” *Advances in Mechanical Engineering*, vol. 9, no. 9, 2017.
- [43] Z. Mu, W. Xu, and B. Liang, “Avoidance of multiple moving obstacles during active debris removal using a redundant space manipulator,” *International Journal of Control, Automation and Systems*, vol. 15, no. 2, pp. 815–826, 2017.
- [44] L. Shi, S. Kayastha, and J. Katupitiya, “Robust coordinated control of a dual-arm space robot,” *Acta Astronautica*, vol. 138, pp. 475–489, 2017.
- [45] M. Andrenucci, P. Pergola, A. Ruggiero, J. Olympio, and L. Summerer, “Active removal of space debris - expanding foam application for active debris removal,” in *62nd International Astronautical Congress*, pp. 1–11, Cape Town, South Africa, 2011.
- [46] P. W. Kelly, R. Bevilacqua, L. Mazal, and R. S. Erwin, “Tugsat: removing space debris from geostationary orbits using solar sails,” *Journal of Spacecraft and Rockets*, vol. 55, no. 2, pp. 437–450, 2018.
- [47] F. Cichocki, M. Merino, and E. Ahedo, “Spacecraft-plasma-debris interaction in an ion beam shepherd mission,” *Acta Astronautica*, vol. 146, pp. 216–227, 2018.
- [48] F. Cichocki, M. Merino, E. Ahedo, M. Smirnova, A. Mingo, and M. Dobkevicius, “Electric propulsion subsystem optimization for “Ion Beam Shepherd” missions,” *Journal of Propulsion and Power*, vol. 33, no. 2, pp. 370–378, 2017.
- [49] W. J. O’Connor and D. J. Hayden, “Detumbling of space debris by a net and elastic tether,” *Journal of Guidance, Control, and Dynamics*, vol. 40, no. 7, pp. 1832–1839, 2017.
- [50] L. Kai-Lei, L. Wen-Hao, Z. Heng, X. Xin-Xin, and G. Zheng-Xiong, “New propulsion technique for leo spacecrafts: magnetism propulsion,” *Journal of Astronautics*, vol. 33, no. 7, pp. 984–990, 2012.
- [51] K. Liu, H. Zhang, W. Li, X. Xiao, and Z. Guo, “The characteristics of geomagnetic field’s gradient distribution and the magnetic force effects in nearearth space,” *Spacecraft Environment Engineering*, vol. 29, no. 5, pp. 479–485, 2012.
- [52] D. W. Kwon, R. J. Sedwick, S.-I. Lee, and J. Ramirez-Riberos, “Electromagnetic formation flight testbed using superconducting coils,” *Journal of Spacecraft and Rockets*, vol. 48, no. 1, pp. 124–134, 2011.
- [53] W. Kwon and M. Daniel, *Electromagnetic Formation Flight of Satellite Arrays*, Massachusetts Institute of Technology, 2005.
- [54] N. A. Matteo and Y. T. Morton, “Ionosphere geomagnetic field: comparison of IGRF model prediction and satellite measurements 1991–2010,” *Radio Science*, vol. 46, no. 4, 2011.

